Simulation of diffusion with non-equilibrium vacancies, Kirkendall shift and porosity in single-phase alloys

Thomas Gheno, Victor Szczepan, Camille Salsi, Clara Desgranges, Daniel Monceau

Simulation of diffusion with non-equilibrium vacancies, Kirkendall shift and porosity in single-phase alloys

Thomas Gheno[a]* , Victor Szczepan[a]†, Camille Salsi[a], Clara Desgranges[b]‡ and Daniel Monceau[c]

[a] *DMAS, ONERA, Université Paris Saclay, F-92322 Châtillon, France*
[b] *Safran Tech, rue des jeunes bois, Châteaufort, F-78772 Magny-les-Hameaux, France*
[c] *CIRIMAT, INP-ENSIACET, 4 allée Emile Monso, F-31030 Toulouse, France*

This is the accepted version of an article published in Computational Materials Science, available at: https://doi.org/10.1016/j.commatsci.2022.111785

Abstract In an alloy subject to vacancy-mediated diffusion, differences in intrinsic diffusivities tend to produce vacancy excess and deficit. These are accommodated by mechanisms such as dislocation climb and pore formation. This is of concern in high temperature alloy-coating systems used in industrial applications, as pores may develop at the interface between the alloy and the coating, which is undesired. This paper presents a multicomponent diffusion model with two types of vacancy sinks/sources: one is associated with dislocation climb and generates lattice shift, the other one is associated with porosity increase/decrease. The model is designed toward a 1D implementation, and porosity is described with a local average volume fraction. Thermodynamic properties and mobility are modeled according to the Calphad method to allow future application to engineering materials. Finite-difference simulations run on two binary systems, NiCr and NiSi, illustrate the role of the two types of sinks in interdiffusion and pore development. Diffusion is found to be more sensitive to the sink strengths in the NiSi system, where intrinsic diffusivities have a stronger composition dependence. This work provides a basis for the evaluation of the parameters involved in vacancy generation/annihilation (e.g. dislocation density) from experimental data, such as concentration profiles obtained from diffusion couple experiments, and for the prediction of porosity in engineering materials.

Keywords Kirkendall effect, lattice shift, porosity, numerical simulation

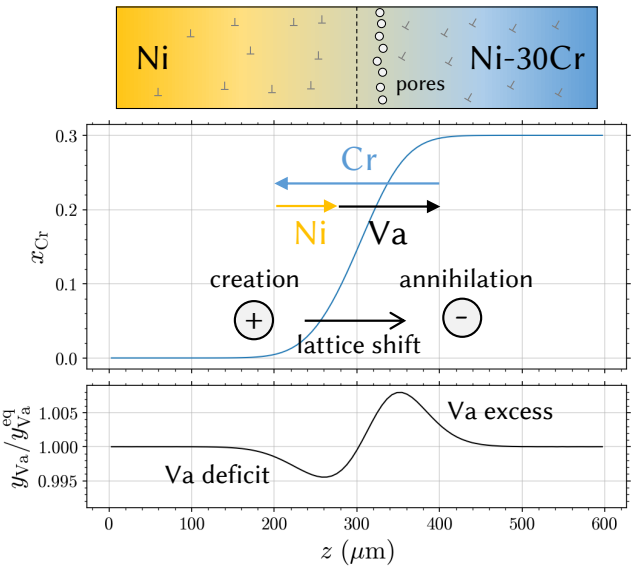

*Corresponding author. Email address: thomas.gheno at onera.fr
†Present address: Safran Tech, rue des jeunes bois, Châteaufort, F-78772 Magny-les-Hameaux
‡Present address: Université Paris-Saclay, CEA, SCCME, F-91191, Gif-sur-Yvette

Nomenclature

a	lattice parameter
c_k^m	concentration of species k (number of moles per unit volume) in the metal phase
c_k	concentration of species k (number of moles per unit volume) in the system
D_k^*	tracer diffusion coefficient of species k
D_k^0	pre-exponential factor in the tracer diffusion coefficient of species k
$\overline{D}_k$	intrinsic diffusion coefficient of species k
f_i	volume fraction of phase i ($i = m$ or p, i.e. metal or pore)
f_0	geometrical correlation factor
G	total Gibbs free energy
G_M	Gibbs free energy per mole of lattice site
G_m	Gibbs free energy per mole of metal species
G_i	Gibbs free energy of endmember i
${}^{xs}G_M$	excess Gibbs free energy per mole of lattice site
$G_{f,Va}^{\text{alloy}}$	vacancy formation energy in the alloy
H	number of jogs per unit volume
J_k^{lab}	flux of species k in the laboratory reference frame
J_k^{lat}	flux of species k in the lattice reference frame
J_k^N	flux of species k in the number-fixed reference frame
k_m	sink strength of the lattice (dislocation climb)
k_p	sink strength of the pores
K	bulk viscosity
L_{ki}	transport coefficient
L_{ki}^m	transport coefficient in the metal phase
L_0	mean free path of vacancies
m_k	atomic mass of species k
M_k	mobility of species k
n_p	average jog spacing (number of sites between jogs)
N_k	number (moles) of species k in the lattice
N	total number (moles) of sites in the lattice
Q_k	activation energy in the tracer diffusion coefficient of species k
r_p	pore radius
r_s	pore spacing
R	ideal gas constant
t	time
T	absolute temperature
v	velocity of the lattice in the laboratory reference frame
W_i	volume of phase i ($i = m$ or p, i.e. metal or pore)
W	volume of the system
x_k	atom fraction of species k
y_k	site fraction of species k
y_0^{eq}	equilibrium site fraction of vacancies
α_m	rate of vacancy annihilation/creation in the lattice (dislocation climb)
α_p	rate of vacancy annihilation/creation due to pore growth/shrinkage
α	total vacancy annihilation/creation rate
α_∞	ideal sink rate (infinite lattice sink strength, vacancies maintained at equilibrium)
γ	surface energy
Δz_i	grid size at position i

${}^{\nu}\Lambda_{ij}$	interaction parameter of order ν between species i and j
μ_k	chemical potential of species k
$\widetilde{\mu}_k$	diffusion potential of species k
ρ_k	mass density of species k
ρ	dislocation density
σ_H	hydrostatic stress
Ω_k	partial molar volume of species k
Ω_m	average molar volume of the metal phase
Ω	average molar volume of the system

1 Introduction

Diffusion simulations have become widely used to predict composition evolutions in high temperature materials, e.g. in alloy-coating systems or in alloys subject to selective oxidation [1–6]. In a substitutional alloy subject to vacancy-mediated diffusion, a composition gradient will generate diffusion, which in turn may have consequences associated with the Kirkendall effect [7–10]. In a composition gradient, the inequality of the atom intrinsic diffusion coefficients causes a flux imbalance and thereby generates a local vacancy flux, which in turn drives the vacancy concentration away from its equilibrium value. Dislocation climb tends to mitigate this non-equilibrium by emitting and absorbing vacancies in undersaturated and supersaturated regions, respectively; this produces a shift of lattice planes relative to each other. Excess vacancies may also condense into pores [11,12], referred to as Kirkendall pores (also called Frenkel pores or voids). Pore surfaces may then act as sinks/sources, resulting in pore growth/decrease. Other manifestations of the Kirkendall effect include stress build-up or specimen bending [13–16].

Darken's theory of diffusion [17], which rationalizes the Kirkendall effect, implicitly assumes that vacancies are maintained at equilibrium, and that this is entirely achieved through lattice shift. This in turns implies that sufficient dislocations are present to accommodate, instantly and everywhere, the vacancy excess/deficit; in other words, the relaxation of vacancies is instantaneous. In the following, this configuration of ideal sinks in the lattice and no porosity is referred to as ideal lattice – and the term sink is used to mean both source and sink.

Several numerical tools used today to simulate interdiffusion [1,2,4,5] rely on Ågren's formalism [18,19], which also considers an ideal lattice and therefore cannot, by construction, generate Kirkendall porosity. Methods were introduced [20–22] to estimate pore fractions as a post-processing step of simulations run in this configuration. This assumes that if allowed to vary, the vacancy concentration would not significantly depart from the equilibrium value, which raises a number of questions. Where pores are present, some supersaturation had to be reached; the minimum level required for a pore to nucleate is not known in general. In vacancy-mediated diffusion, transport coefficients depend on the local vacancy concentration [18]. It is therefore expected that atom concentration profiles differ depending on whether vacancies are maintained at equilibrium or not. Balluffi [12] argued that the relative supersaturation ($R = (C_{Va} - C_{Va}^{eq})/C_{Va}^{eq}$, where C_{Va} is the number of vacancies per unit volume) required for pore nucleation could not be large, and provided an

order of magnitude estimate of the upper limit: $R \leq 10^{-2}$. It is desirable to confirm this figure with a more quantitative approach, and to evaluate the impact such supersaturation would have on concentration profiles in alloy systems of interest.

A variety of multicomponent diffusion models with non-ideal sinks, giving rise to non-equilibrium vacancies, have been developed by previous investigators [11,13,23–36]. These consider a continuity equation for vacancies, where the sink term is modeled with a finite strength (or equivalently, a non-zero relaxation time), which reflects the limited ability of the lattice to annihilate vacancies. Svoboda et al. associated vacancy generation and molar volume variations with creep [28], and developed sink models corresponding to different crystal defects (dislocation jogs, Frank loops, grain boundaries) [37]. Gusak and Storozhuk [31] studied the simultaneous action of lattice sinks, modeled as a uniform distribution with prescribed strength, and pores, modeled as discrete spheres. The authors made simplifying assumptions to keep the problem tractable analytically – the two types of sinks were treated at different space scales, in a quasi-steady-state regime. These were partially lifted in Refs. [33,35], where the problem was studied numerically. Yu et al. studied the case of a perfect lattice (no sink, i.e., conserved vacancies) with grain boundaries acting as discrete, ideal sinks [29]. The same group studied pore formation in 2D geometries, with free surfaces acting as ideal sinks, and a lattice with either no sink [38] or ideal sinks [39].

In most of the cases cited above, numerical simulations were applied to a thermodynamically ideal alloy system with composition-independent mobilities, using arbitrary parameters rather than parameters optimized from experimental data. This, of course, is very valuable to study the essential features of diffusion, but applications to systems with quantitative data have been lacking. Fischer and Svoboda [40] did study the Fe-Cr-Ni system with an assessed thermodynamic description, but the mobility and equilibrium vacancy fraction were set as composition-independent. As we shall show, the composition dependence of mobilities plays a significant role in the system evolution. More recently, Xia et al. [36] used a thermodynamic model that includes atom-vacancy interaction parameters and allows for composition-dependent equilibrium vacancy fraction. Their work includes non-ideal lattice sinks, giving rise to non-equilibrium vacancies, but computes pore fractions as a post-processing step, and therefore does not consider the possible interactions between lattice sinks and pores.

Our objective is to study the role of lattice sinks and pores on the composition during interdiffusion, including the interactions between the two types of sinks, and to examine how this diffusion behavior is affected by the diffusion properties of the system. For this purpose, we build a diffusion model with dislocation climb and pore growth acting as two separate, non-ideal vacancy sinks. The thermodynamic properties and mobility are modeled according to the Calphad method [41,42] to facilitate the use of critically assessed data and future application to engineering materials. The model is at present limited to substitutional diffusion in single-phase alloys.

The mechanisms underlying vacancy annihilation/creation are complex, and sink strengths cannot be determined a priori for any given microstructure or chemical composition. In the present paper, diffusion couple simulations are run with a broad range of sink strength values. We then examine the influence of lattice and pore sink strength on quantities that can be measured experimentally (atom fraction and pore

profiles). This approach can be used to estimate sink strengths from experimental data.

The paper starts with a description of the models and numerical schemes. We then presents the results of parametric studies on systems with a weaker Kirkendall effect (NiCr) and with a stronger Kirkendall effect (NiSi). Finally, the influence of the sink terms is discussed in light of sink models available in the literature.

2 Models

2.1 Composition variables

The system composition is described using the formalism of Svoboda et al. [26,28] restricted to substitutional species, and modified to include porosity. Let W be a representative volume comprising a crystalline solid (metal) and pores:

$$W = W_m + W_p \ . \tag{1}$$

Within W, metal and pores are not spatially resolved; we consider the average properties of the volume.

The metal is a disordered solid solution, with a single sublattice. It contains N mol of lattice sites, occupied by atoms and vacancies:

$$N = \sum_{k=0}^{n} N_k \ , \tag{2}$$

In Eq. (2), N_k is the quantity (mol) of species k, where index 0 represents vacancies and indices 1 to n represent atoms. Site fractions y_k are defined as

$$y_k = \frac{N_k}{N}, \ k \in [0, n] \, , \tag{3}$$

and verify

$$\sum_{k=0}^{n} y_k = 1. \tag{4}$$

Atom fractions are defined as

$$x_k = \frac{y_k}{1 - y_0} \ , \ k \in [1, n] \tag{5}$$

for atoms, and verify

$$\sum_{k=1}^{n} x_k = 1. \tag{6}$$

Vacancies do not have a atom fraction. The average molar volume of the metal, Ω_m, is defined as

$$\Omega_m = \sum_{k=1}^{n} x_k \Omega_k \ , \tag{7}$$

where Ω_k is the partial molar volume of species k, assumed to be constant. Equation (7) is obtained by considering that the partial molar volume of the vacancies is

the molar volume of the metal, $\Omega_0 = \Omega_m$, see Ref. [28]. Concentrations (mol m^{-3}) in the metal are given by

$$c_k^m = \frac{y_k}{\Omega_m}, \ k \in [0, n] \, . \tag{8}$$

The volume occupied by the metal is

$$W_m = N\Omega_m \ . \tag{9}$$

The pores contain no site; the number of sites in W is that of the metal, N. The global molar volume Ω is defined such that

$$W = N\Omega \ . \tag{10}$$

Volume fractions are defined as

$$f_i = \frac{W_i}{W}, \quad i = m \text{ or p.} \tag{11}$$

It follows that the global molar volume is related to the metal molar volume through

$$\Omega = \frac{\Omega_m}{f_m} \ . \tag{12}$$

Global concentrations (mol m^{-3}) are given by

$$c_k = \frac{y_k}{\Omega} = c_k^m \cdot f_m \ , \tag{13}$$

and verify

$$\sum_{k=0}^{n} c_k = \frac{1}{\Omega} \ . \tag{14}$$

2.2 Thermodynamics of the metal phase

The thermodynamic properties of the metal phase are modeled according to the Calphad method. The Gibbs free energy per mole of lattice site is written [41,42]

$$G_M = \sum_{i=0}^{n} y_i G_i + RT \sum_{i=0}^{n} y_i \ln y_i + {}^{xs}G_M \ , \tag{15}$$

where G_i is the Gibbs energies of endmember i (0 represents vacancies, indices 1 to n represent atoms), R and T have their usual meaning and ${}^{xs}G_M$ is the excess term. The latter is modeled using a Redlich-Kister polynomial . Considering only binary interactions, this reads [41,42]

$${}^{xs}G_M = \sum_{i=0}^{n-1} \sum_{j=i+1}^{n} y_i y_j \sum_{\nu=0}^{m} {}^{\nu}\Lambda_{\mathrm{ij}} \left(y_i - y_j\right) \tag{16}$$

The binary interaction terms, ${}^{\nu}\Lambda_{\mathrm{ij}}$, are expressed in the form $A + B \cdot T$.

Two quantities deriving from the Gibbs free energy are needed in the diffusion simulations: chemical potentials and the equilibrium vacancy fraction. The former are defined as [42]

$$\mu_k = \frac{\partial G}{\partial N_k} \ , \tag{17}$$

where G is the total Gibbs free energy, $G = N \cdot G_M$. For example, with a regular solution model (${}^{xs}G_M = \sum_{i=0}^{n-1} \sum_{j=i+1}^{n} y_i y_j \Lambda_{\mathrm{ij}}$), one finds

$$\mu_k = G_k + RT \ln y_k + \sum_{j=0}^{n} (1 - \delta_{\mathrm{jk}})\, y_j \Lambda_{\mathrm{jk}} - \sum_{i=0}^{n-1} \sum_{j=i+1}^{n} y_i y_j \Lambda_{\mathrm{ij}}, \tag{18}$$

where $\delta_{\mathrm{jk}} = 1$ if $j = k$, and 0 otherwise.

The equilibrium vacancy fraction in the metal is obtained by solving the equilibrium between the metal and a vacancy-rich phase (a pore), which, making use of the approximation $y_0 \ll 1$, leads to the condition

$$\mu_0 = 0 \tag{19}$$

(see derivation in Appendix A). Again taking the example of a regular solution model, y_0^{eq} then verifies:

$$G_0 + RT \ln y_0^{eq} + \sum_{i=1}^{n} y_i \Lambda_{0i} - \sum_{i=1}^{n-1} \sum_{j=i+1}^{n} y_i y_j \Lambda_{\mathrm{ij}} = 0. \tag{20}$$

This can be written

$$y_0^{eq} = \exp\left(-\frac{G_{f,Va}^{\mathrm{alloy}}}{RT}\right), \tag{21}$$

where

$$G_{f,Va}^{\mathrm{alloy}} = G_0 + \sum_{i=1}^{n} y_i \Lambda_{0i} - \sum_{i=1}^{n-1} \sum_{j=i+1}^{n} y_i y_j \Lambda_{\mathrm{ij}} \tag{22}$$

is the vacancy formation energy in the alloy. Different expressions for Eqs. (18) and (22) would be obtained with a different solution model. In any case, in a non-ideal alloy, the equilibrium vacancy fraction is composition-dependent. The chemical potential of vacancies can always be written in the form:

$$\mu_0 = RT \cdot \ln\left(\frac{y_0}{y_0^{eq}}\right) . \tag{23}$$

While the Gibbs energies of the metal end-members can readily be calculated from parameters in the literature, the Gibbs energy of the vacancy endmember, i.e., of a lattice with no atoms, has no trivial definition. A common practice is to choose a value arbitrarily to ensure the existence and uniqueness of an equilibrium state between the metal and the pore, as discussed by multiple investigators [43]–[49]. Here we follow the recommendation of Franke [45] and use $G_{Va} = RT(\ln 2 - 1/2)$. The value of G_{Va} has no significant impact on the simulation results.

Likewise, atom-vacancy interaction parameters are not generally known. Following Abe et al. [48], we assume 0-order binary interactions, and the interaction parameters are determined based on the vacancy formation energy in pure metals: $\Lambda_{k0} = G_{f,Va}^{k} - G_{Va}$ (see derivation in Appendix B).

2.3 Metal-pore equilibrium

Multiphase diffusion simulations typically rely on local equilibrium to compute phase compositions and fractions from global compositions given by the continuity equation. Modeling the energetics of the pore phase with an ad-hoc Gibbs energy function is not trivial, and is avoided here. The present model is designed for a one-dimension implementation, and does not consider metal and pores as spatially resolved phases but simply includes their contributions to the system composition through their average volume fraction. As described in Section 2.5, the lattice sink rate is modeled as proportional to the difference between the vacancy fraction and the equilibrium vacancy fraction in the metal. The latter can be computed for any given metal composition by solving $\mu_0 = 0$, as described above. The remaining degree of freedom, the pore fraction, will be handled in a similar fashion (Section 2.5).

2.4 Mobility

Situations of interest commonly involve diffusion in one dimension and invariance by translation in the other two. Our model is therefore designed towards a planar 1D implementation, and assumes that deformation is constrained to a 1D incompressible plastic flow, which results in the absence of stress.

Mass transport may be split into diffusive and advective fluxes. Several formalisms have been used to distinguish these contributions in the literature, such as Lagrangian and Eulerian coordinate systems [13] or actual and reference configurations [26]. In the present work, flux densities are described using two reference frames: (i) the lattice reference frame, based on a local coordinate system attached to inert markers in the lattice, and (ii) the laboratory reference frame, based on a global coordinate system that coincides with the lattice reference frame at $t = 0$ but does not deform thereafter. The lattice moves with respect to the laboratory reference frame with a velocity field v. The fluxes of species k in the lattice and laboratory reference frames, noted J_k^{lat} and J_k^{lab} respectively, are related by

$$J_k^{lab} = J_k^{lat} + c_k \cdot v \ , \tag{24}$$

where we recognize diffusive (J_k^{lat}) and advective ($c_k \cdot v$) contributions. J_k^{lat} is written [10]

$$J_k^{lat} = -\sum_{i=0}^{n} L_{ki} \ \mathrm{grad}\ \mu_i \ , \tag{25}$$

where the L_{ki} are the transport coefficients (also called Onsager coefficients), which form a symmetric matrix. Lattice sites are conserved by substitutional diffusion:

$$\sum_{k=0}^{n} J_k^{lat} = 0. \tag{26}$$

(this is true even if lattice sites are not conserved overall due to the action of sinks). This allows the vacancy flux to be expressed as a function of n independent atom fluxes, and all L_{k0} to be expressed as a function of the atom transport coefficients, which are related to measurable mobilities. After some manipulation one obtains

$$J_k^{lat} = -\sum_{i=1}^{n} L_{ki} \ \mathrm{grad}\ \widetilde{\mu}_i \ , \tag{27}$$

where $\widetilde{\mu}_i$ is the diffusion potential, defined as $\widetilde{\mu}_i = \mu_i - \mu_0$ (see derivation in Appendix C).

With regards to porosity, like Audigié's thesis [34], we are interested in simulating average pore fractions rather than individual, spatially resolved pores. The L_{ki} then reflect diffusional transport in the metal + pores system, and we assume these can be expressed as a weighted average of transport coefficients in the metal and in the pores:

$$L_{ki} = f_m L^m_{ki} + f_p L^p_{ki} \ . \tag{28}$$

We further assume $L^p_{ki} = 0 \ \ \forall(k,i)$, i.e., no diffusion in the pores. This yields:

$$L_{ki} = f_m L^m_{ki} \ , \tag{29}$$

where L^m_{ki} are the transport coefficients in the metal. Following Ågren [18], we consider the vacancy-exchange mechanism, in which diffusion occurs by atoms jumping into neighboring vacant sites, and vacant sites are distributed randomly. The transport coefficients are then expressed as

$$\begin{cases} L^m_{kk} = c^m_k y_0 M_{k0} \\ L^m_{ki} = 0 \qquad \text{for } k \neq i, \end{cases} \tag{30}$$

where M_{k0} is a kinetic parameter representing the rate of exchange between a k atom and a neighboring vacancy. The mobility of species k is then [19]

$$M_k = y_0 M_{k0} \ . \tag{31}$$

The mobility is related to the tracer diffusion coefficient D^*_k by Einstein relation:

$$M_k = \frac{D^*_k}{RT} \ . \tag{32}$$

Here, we follow Ågren [18] and set the off-diagonal transport coefficients to 0, instead of using Manning's random alloy model [50] for instance, because simulations will be run using mobility parameters optimized from experimental data, where in all cases known to us, the optimization was done with $L^m_{ki} = 0$ for $k \neq i$.

Tracer experiments measure solute diffusion in the dilute regime, where the Kirkendall effect is negligible. It is therefore assumed that D^*_k reflects the diffusion of k in a solution with an equilibrium vacancy fraction, and it follows that mobilities evaluated from tracer diffusion coefficients are equilibrium mobilities, i.e.,

$$\frac{D^*_k}{RT} = M^{eq}_k = y^{eq}_0 M_{k0}. \tag{33}$$

If we further assume that non-equilibrium vacancy fractions arising from the Kirkendall effect in the concentrated regime remain sufficiently close to equilibrium values, the same exchange coefficient M_{k0} applies to both equilibrium and non-equilibrium situations. Consequently, the mobility can be written with the general form:

$$M_k = \frac{y_0}{y^{eq}_0} M^{eq}_k. \tag{34}$$

Using Eqs. (27)–(34), the fluxes are finally written

$$J^{lat}_k = -L_{kk} \ \text{grad} \ \widetilde{\mu}_k, \tag{35}$$

with

$$L_{kk} = f_m c_k^m \frac{y_0}{y_0^{eq}} \frac{D_k^*}{RT} = c_k \frac{y_0}{y_0^{eq}} \frac{D_k^*}{RT} \ . \tag{36}$$

The temperature dependence of tracer diffusion coefficients is described with the Arrhenius relation

$$D_k^* = D_k^0 \exp\left(-\frac{Q_k}{RT}\right), \tag{37}$$

where D_k^0 is the preexponential factor and Q_k the activation energy. Following a common practice in the mobility literature, Eq. (37) is expressed as:

$$\ln D_k^* = \frac{\phi_k}{RT} \ , \tag{38}$$

with $\phi_k = RT \ln D_k^0 - Q_k$. The composition dependence is then given by expanding ϕ_k with a Redlich-Kister polynomial, see Eq. (16).

2.5 Diffusion

The system of continuity equations in the laboratory reference frame is:

$$\begin{cases} \dfrac{\partial c_k}{\partial t} = -\text{div} \ \left(J_k^{lat} + c_k v\right) & (k > 0) \\ \dfrac{\partial c_0}{\partial t} = -\text{div} \ \left(J_0^{lat} + c_0 v\right) + \dfrac{1}{\Omega} \dfrac{\dot{N}}{N} \end{cases} \tag{39}$$

(see derivation in Appendix D). Equation (39) reflects the fact that atom concentrations vary because of diffusion and advection, while the vacancy concentration additionally changes due via the sink term $\dot{N}/N$. The notations $\frac{\partial X}{\partial t}$ and $\dot{X}$ are used to denote time derivatives in the laboratory reference frame and in the lattice reference frame, respectively (see Appendix D). The velocity field is evaluated from its divergence (Appendix D):

$$\text{div} \ v = f_m \left(\frac{\dot{N}}{N} + \frac{\dot{\Omega}_m}{\Omega_m}\right) + f_p \frac{\dot{W}_p}{W_p} \ . \tag{40}$$

Evaluating div v requires a sink model. Following Ref. [28], we note the sink term $\alpha = \dot{N}/N$. As is commonly done in the literature [10], we use a linearized form and assume α is proportional to $y_0 - y_0^{eq}$. We further postulate that α can be expressed as the sum of two contributions, due to lattice sinks and pores:

$$\begin{cases} \dfrac{\dot{N}}{N} = \alpha = \alpha_m + \alpha_p \\ \alpha_m = -k_m \left(y_0 - y_0^{eq}\right) \\ \alpha_p = -k_p \left(y_0 - y_0^{eq}\right). \end{cases} \tag{41}$$

In Eq. (41), k_m and k_p (unit s^{-1}) are the sink strengths and reflect both the sink densities and the frequency at which they operate; these parameters may depend on alloy composition and microstructure. The index m refers to lattice sinks, i.e.,

dislocation climb: α_m produces the Kirkendall shift. The index p refers to pores. The rate of pore volume variation is written:

$$\dot{W}_p = -N\alpha_p\Omega_0 \ . \tag{42}$$

Recalling the hypothesis $\Omega_0 = \Omega_m$ (see Section 2.1), this yields

$$\frac{\dot{W}_p}{W_p} = -\frac{f_m}{f_p}\alpha_p \ . \tag{43}$$

The variation rate of the metal molar volume is obtained by deriving Eq. (7) and making use of the expression of $\dot{y}_k$ (Eq. (D.2) in Appendix D):

$$\frac{\dot{\Omega}_m}{\Omega_m} = \frac{1}{f_m(1-y_0)}\sum_{k=1}^{n}(\Omega_m - \Omega_k)\,\mathrm{div}\ J_k^{lat}. \tag{44}$$

Finally, the divergence of the velocity field is:

$$\mathrm{div}\ v = f_m\alpha_m + \frac{1}{1-y_0}\sum_{k=1}^{n}(\Omega_m - \Omega_k)\,\mathrm{div}\ J_k^{lat} \ . \tag{45}$$

Equation (45) reflects the fact that the system deformation stems from two contributions: the action of lattice sinks (Kirkendall shift) and the differences between partial molar volumes.

2.6 Limiting case: ideal lattice

The ideal lattice configuration, where lattice sinks are sufficiently active to maintain vacancies at equilibrium without forming pores, may be represented by $k_m = +\infty$. If y_0^{eq} is composition-independent, and assuming that initially $y_0 = y_0^{eq}$, the corresponding sink rate, noted α_∞, can be obtained analytically by solving

$$\dot{y}_0 = 0. \tag{46}$$

Using the expression for $\dot{y}_0$ (Eq. (D.2) in Appendix D), this yields

$$\alpha_\infty = \frac{\Omega}{1-y_0^{eq}}\ \mathrm{div}\ J_0^{lat}. \tag{47}$$

Substituting $\alpha_m = \alpha_\infty$ and $f_m = 1$ in Eq. (45), the divergence of the velocity field is

$$\mathrm{div}\ v = \frac{\Omega}{1-y_0^{eq}}\ \mathrm{div}\ J_0^{lat} + \frac{1}{1-y_0^{eq}}\sum_{k=1}^{n}(\Omega_m - \Omega_k)\,\mathrm{div}\ J_k^{lat}. \tag{48}$$

In the case where all partial molar volumes are equal, $\Omega_k = \Omega_m \ \ \forall k$, the right hand side term in Eq. (48), which corresponds to the lattice deformation due to molar volume variations, vanishes. If y_0^{eq} is composition-independent, in 1D, Eq. (48) can be integrated to yield the velocity at position z:

$$v = \frac{\Omega}{1-y_0^{eq}}\ \left[\ J_0^{lat}\right]_{z_{\min}}^{z} \ . \tag{49}$$

Under the additional conditions that $y_0^{eq} \ll 1$ and $J_0^{lat} = 0$ at the left-hand side border of the simulated domain ($z = z_{\min}$), Eq. (49) finally yields:

$$v = -\Omega \sum_{k=1}^{n} J_k^{lat}. \tag{50}$$

The number-fixed reference frame is defined as the frame in which the fluxes, noted J_k^N, verify:

$$\sum_k J_k^N = 0. \tag{51}$$

Since, in the present Section, we assume Ω is constant, the volume-fixed reference frame is identical to the number-fixed reference frame [18]. The velocity of any reference frame (where fluxes are noted $J_k^{'}$) relative to the number-fixed reference frame is given by [18]:

$$v = -\Omega \sum_k J_k^{'}. \tag{52}$$

This relation applies to the lattice reference frame. By analogy with Eq. (50), we conclude that under all the conditions listed in this Section (y_0^{eq} is composition-independent, $y_0^{eq} \ll 1$, $y_0 = y_0^{eq}$ initially, $\Omega_k = \Omega_m \quad \forall k$, $J_0^{lat}(z_{\min}) = 0$), the laboratory reference frame coincides with the volume-fixed reference frame in which vacancies are not considered. The latter configuration is the one used in Ågren's formalism [18,19] and in many commercial and academic diffusion codes used to simulate engineering materials.

3 Implementation and data

The models are implemented in Python, via scripts that heavily rely on the Numpy [51] and Scipy [52] libraries. All plotting is done with Matplotlib [53]. The source code will be distributed under an open license. The documentation will contain more implementation details than can be included here.

3.1 Thermodynamics

Simulations are run on fcc, Ni-based alloys. The atom-vacancy interaction parameters are obtained from the energy of formation of vacancies in pure metals in the fcc crystal structure. These cannot necessarily be measured experimentally, and indeed experimental data of this type are scarce even when the pure metal is stable in the fcc structure. Instead, we use DFT results from Shang et al [54] (from their Supplementary Data), which provide a consistent dataset for most elements of interest. When the vacancy formation energy for a given element is not given in Ref. [54], we use the value for Ni instead.

Gibbs energies of pure metals and atom-atom interaction parameters are obtained from assessed descriptions of the relevant systems published in the literature. These are available as functions of atom fractions, not site fractions, i.e., instead of Eq. (15), the data are based on:

$$G_M\left(\ldots x_i \ldots\right) = \sum_{i=1}^{n} x_i G_i + RT \sum_{i=1}^{n} x_i \ln x_i + {}^{xs}G_M\left(\ldots x_i \ldots\right). \tag{53}$$

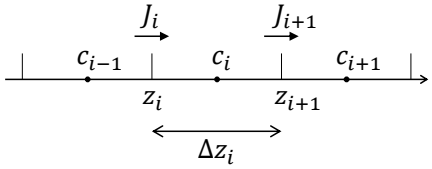

Figure 1: Space discretization scheme.

In principle, a conversion is required from the atoms description, $G_M(\dots x_i \dots)$, to the atoms + vacancy description of Eq. (15), $G_M(\dots y_i \dots)$. However, as noted in Section 2.2, we assume $y_0 \ll 1$, and therefore $y_k \cong x_k$. Consequently, we use Eq. (53) to obtain interaction parameters, and assume these would be the same as those obtained with Eq. (15), i.e., we use these parameters in Eq. (15) to compute equilibrium vacancy fractions and chemical potentials.

Similarly, calculating the equilibrium vacancy fraction using Eqs. (21)-(22) requires the system composition to be described in terms of site fractions. Most often, however, one needs to calculate y_0^{eq} in a metal whose composition is known as mole fractions of the metal species, not site fractions. Obtaining y_k from x_k requires y_0, which is the unknown quantity. However, the assumption $y_0 \ll 1$ implies $y_k \cong x_k, \quad k \in [1, n]$. It follows that y_0^{eq} can be directly computed from atom fractions, without the need for an iterative scheme to solve Eq. (21).

3.2 Mobility

The parameters describing the composition dependence of ϕ_k in Eq. (38) are obtained from the literature. These are available in terms of atom fractions: $\phi_k = \phi_k(\dots x_i \dots)$. In the case of the mobility parameters, however, functions of site fractions are not needed. The $\phi_k(\dots x_i \dots)$ models from the literature are directly used to calculate tracer diffusion coefficients with Eq. (38). Non-equilibrium vacancy fractions are taken into account when calculating L_{kk} via Eq. (36).

3.3 Diffusion

The time evolution of the system composition is described by Eq. (39). This is solved using an explicit (forward Euler) finite difference scheme, in one dimension of space. The total length is divided into segments of size Δz_i separated by grid points at positions z_i. The composition variables (x_k, y_k, c_k, Ω_m, Ω, f_m, μ_k) are associated with positions $z_i + \Delta z_i/2$, and represent the average system composition in the Δz_i segments; the fluxes (and the velocity field) are evaluated on grid points z_i: J_i^{lat} represents a flux between segments Δz_{i-1} and Δz_i. The discretization is illustrated in Figure 1. Fluxes are discretized using the arithmetic mean of neighboring L_i and Δz_i values, i.e., Eq. (35) is implemented as:

$$J_i^{lat} = -\left(L_{i-1} + L_i\right) \frac{\widetilde{\mu}_i - \widetilde{\mu}_{i-1}}{\Delta z_{i-1} + \Delta z_i}. \tag{54}$$

(In Eq. (54), indices refer to positions on the grid, not chemical species). Linear interpolation is used when concentrations need to be evaluated on grid points.

The initial conditions comprise profiles of the atom fractions x_k, vacancy site fraction y_0 and metal volume fraction f_m. These are used to compute y_k, Ω_m, and then Ω and finally c_k through the composition relationships in Section 2.1.

The divergence of the velocity field is determined via Eq. (45). In principle, a large vacancy undersaturation would lead to a large positive value for α_p in Eq. (41), which could in turn result in a negative pore fraction. In order to avoid this, α_p is capped at an $\alpha_p^{\max}$ value, calculated at every time step from the condition $f_p^{n+1} \geq 0$. The velocity is obtained by integrating its divergence along the space dimension, where the integration constant $v(z_{\min})$ depends on the boundary condition.

The velocity field is then used to compute the time derivatives in Eq. (39). The $n+1$ concentrations are related through Eq. (14). However, the average molar volume Ω may vary over time, due to the variation of the metal molar volume and volume fraction. Obtaining one of the concentrations through the n others and Eq. (14) would therefore require that the time evolution of Ω be determined independently. Alternatively, we solve Eq. (39) for all $n+1$ concentrations, and then use Eq. (14) to obtain Ω. The c_k and Ω values are then used to compute y_k, then Ω_m and f_m.

3.4 Limiting case: ideal lattice

As discussed in Section 2.6, the ideal lattice configuration, represented here by $k_m = \infty$, is of particular interest for comparison with the literature. This is readily implemented if y_0^{eq} is constant, using Eq. (47) instead of Eq. (41) to compute α_∞. In the present work, however, y_0^{eq} is derived from the Gibbs free energy of the metal, and is composition-dependent (see Section 2.2). An alternative method must therefore be implemented to compute α_∞. The solution retained here is to first assume that y_0^{eq} is constant, compute α_∞ via Eq. (47), and solve the continuity equation on this basis, to obtain a virtual c_k^{n+1}. Then, a virtual y_0^{eq} is calculated from this c_k^{n+1}, and a corrected α is calculated such that $y_0^n + \Delta t \cdot \dot{y}_0 = y_0^{eq}$. The continuity equation is then solved using the corrected α. The new y_0^{eq} will necessarily differ from the one calculated in the virtual step; however, the method produces values of y_0 typically within $10^{-13} - 10^{-14}$ of y_0^{eq}, which is a satisfying approximation.

3.5 Initial and boundary conditions

All simulations presented in Section 4 represent diffusion couple experiments in initially pore-free metal alloys, defined by the following initial conditions: $x_{1..n}$ given by an Heaviside step function; $y_0 = y_0^{eq}(x_{1..n})$; $f_m = 1$ in all regions;

and the boundary conditions $J_k^{lat} = 0 \ \ \forall k$ at $z = z_{\min}$ and $z = z_{\max}$. The simulated domains are discretized into linear grids with 100 steps, which yields step sizes of 6 µm (Section 4.1) and 10 µm (Section 4.2). The time step is chosen to guarantee the stability of the explicit resolution scheme. The small vacancy fraction places a strong constraint on Δt; even smaller Δt values are required when using large values of k_m or k_p to avoid negative vacancy fractions in vacancy annihilation regions. These constraints result in Δt about 10^{-3} to 10^{-2} s in the present conditions.

The partial molar volumes of the atoms are calculated as $\Omega_k = m_k/\rho_k$, where m_k is the atomic mass and ρ_k the mass density. This yields Ω_k values of $6.6 \cdot 10^{-6}$, $7.3 \cdot 10^{-6}$ and $1.2 \cdot 10^{-5}$ m^3/mol for Ni, Cr and Si, respectively.

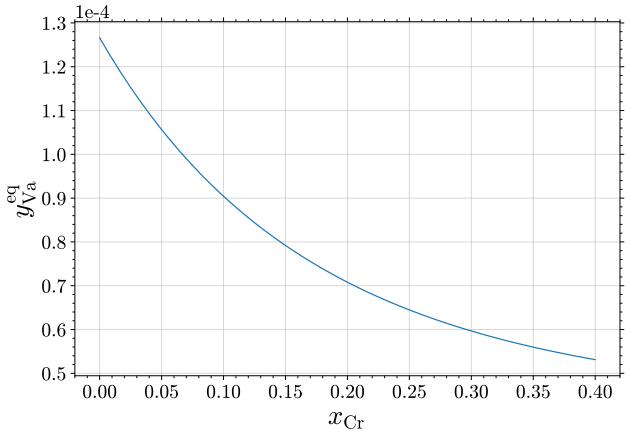

Figure 2: Equilibrium vacancy fraction in the Ni-Cr system at 1200 °C, computed via Eqs. (21)–(22), using atom-vacancy interaction parameters from Shang et al [54] and Ni-Cr data from Lee [55].

4 Results

The influence of dislocation climb and porosity increase/decrease as a vacancy sink/source was studied by running simulations with multiple values of the sink strengths k_m and k_p. The values used were 0, 10^{-2}, 10^{-1}, 1, 10, 10^2 and 10^3 s^{-1}. This produced 49 k_m,k_p combinations. The case of an ideal lattice, where the vacancy concentration is maintained at equilibrium and no pore is formed ($k_m = +\infty$), was also studied. In total, 50 simulations were run for each system.

4.1 Binary system with weak Kirkendall effect: NiCr

Simulations in the NiCr system were conducted using thermodynamic data from Lee [55] and mobility data from Jönsson [56]. Figures 2 and 3 show the equilibrium vacancy fraction and the tracer and intrinsic diffusion coefficients of Cr and Ni at 1200 °C, respectively. In a binary system, intrinsic coefficients are defined as [19]:

$$\overline{D}_k = L_{kk} \frac{\partial \mu_k}{\partial c_k}. \tag{55}$$

Intrinsic coefficients combine mobility and thermodynamic contributions to diffusivities and indicate how fluxes will develop in response to a concentration gradient. The relative $\overline{D}_k$ values provide indications as to the amplitude of the Kirkendall effect. Here, each of $\overline{D}_{\mathrm{Cr}}$ and $\overline{D}_{\mathrm{Ni}}$ is almost constant over the composition range of interest ($\max(\overline{D}_k)$ / $\min(\overline{D}_k) \cong 1.1$ for Cr as well as Ni). The $\overline{D}_{\mathrm{Cr}}/\overline{D}_{\mathrm{Ni}}$ ratio is about 2, which is close to unity, relatively to other systems of interest. Therefore, the Kirkendall effect is expected to be weak and uniform in diffusion couples in the NiCr system.

Simulations were done for a Ni/Ni-30Cr (at. %) diffusion couple, 10 h at 1200 °C, with varying values of the sink strengths, k_m and k_p. The results obtained with no porosity ($k_p = 0$) are presented first.

Figure 4 presents profiles of the Cr atom fraction, fluxes in the lattice reference frame and vacancy relative deviation from equilibrium obtained with $k_p = 0$. With

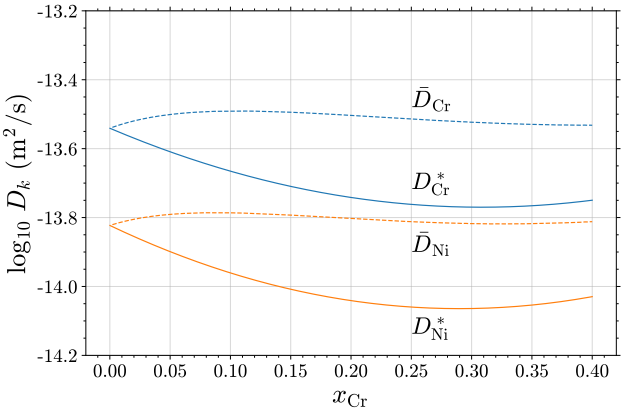

Figure 3: Tracer and intrinsic diffusion coefficients in the Ni-Cr system at 1200 °C, computed using data from Lee [55] and Jönsson [56].

an ideal lattice ($k_m = +\infty$), the shape of the x_{Cr} profile is nearly symmetric (Figure 4(a)), i.e., close to the error function analytical solution that would be obtained with composition-independent diffusivities. This is due to the weak composition dependence of Cr and Ni diffusivities. The flux of Cr is twice as large as that of Ni (Figure 4(b)), which reflects the $\overline{D}_{\mathrm{Cr}}/\overline{D}_{\mathrm{Ni}}$ ratio. As a consequence, J^{lat}_{Va} has the same sign and nearly the same amplitude as J^{lat}_{Ni}. The vacancy fraction is maintained at its equilibrium value in all regions, as expected (Figure 4(c)).

Decreasing the lattice sink strength results in vacancy supersaturation on the Cr-rich side, as annihilation is not fast enough to maintain the vacancy fraction at equilibrium. In a symmetric manner, the Cr-lean side is a region of vacancy generation ($\mathrm{div}\left(J^{lat}_{Va}\right) < 0$); decreasing k_m produces vacancy undersaturation. The vacancy fraction obtained with lower k_m values (10^{-2} and 0 in Figure 4(c)) does not fall back to the equilibrium value within the bounds of the simulation box. This indicates that the latter is too small to represent an infinite media; in particular, this implies that the results depend on the size of the box.

The amplitude of J^{lat}_{Va} is seen to decrease with decreasing k_m, until it reaches 0 in all regions for $k_m = 0$ (Figure 4(b)). The reduction of the vacancy flux is caused by the vacancy accumulation/depletion process: as the $y_{Va} - y^{eq}_{Va}$ gradient develops between the Cr-rich and Cr-lean sides of the couple (Figure 4(c)), it produces a μ_{Va} gradient (μ_{Va} profiles, not plotted here, are homologous to $(y_{Va} - y^{eq}_{Va})/y^{eq}_{Va}$ profiles, see Eq. (23)), which provides a driving force for J^{lat}_{Va} that opposes the driving force due to the difference between J^{lat}_{Cr} and J^{lat}_{Ni}, i.e., the driving force associated with the Kirkendall effect. Since the three fluxes are related (Eq. (26)), the lower amplitude of J^{lat}_{Va} leads to a decrease of J^{lat}_{Cr} and an increase of J^{lat}_{Ni}, until the amplitude of J^{lat}_{Cr} and J^{lat}_{Ni} coincide for $k_m = 0$: Cr and Ni diffuse at the same rate. In other words, the slowness of vacancy generation inhibits the Kirkendall effect generated by the difference between $\overline{D}_{\mathrm{Cr}}$ and $\overline{D}_{\mathrm{Ni}}$.

The case of the NiCr system is particular in that $\overline{D}_{\mathrm{Cr}}$ and $\overline{D}_{\mathrm{Ni}}$ are relatively close to each other, and as a result the Kirkendall effect is weak, even when the lattice sink strength is infinite. It follows that the effects of k_m variations discussed above have no visible manifestation in the Cr atom fraction profile, which remains

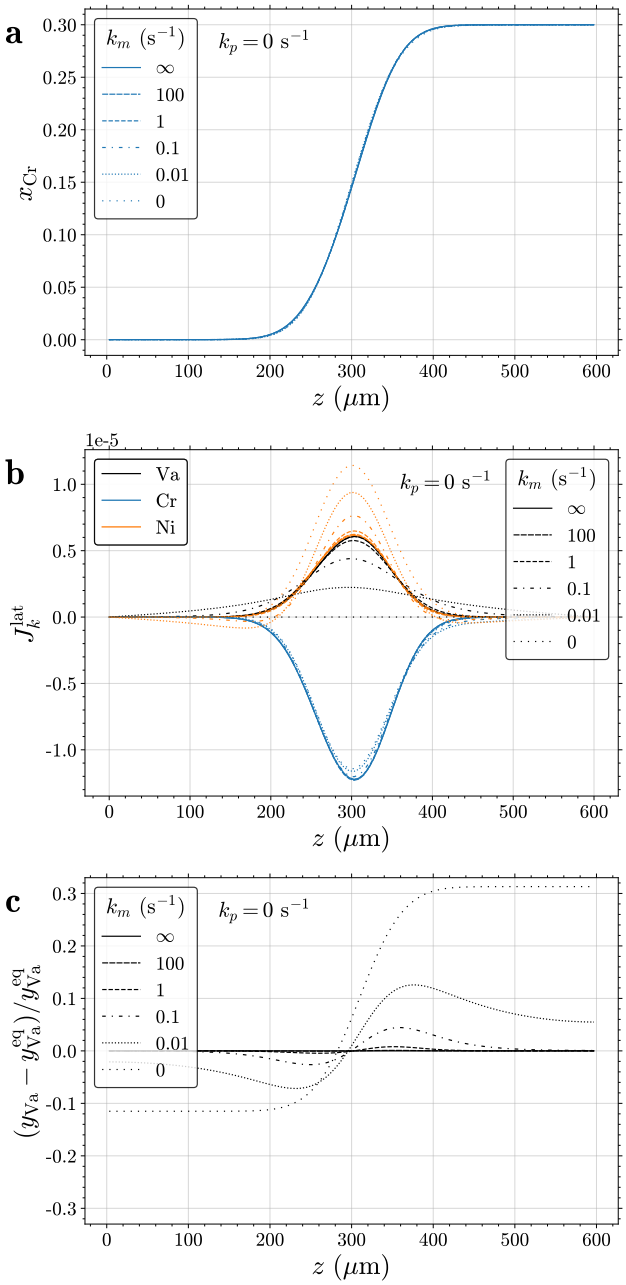

Figure 4: Simulation results for a Ni / Ni-30Cr (at. %) couple, after 10 h at 1200 °C, with $k_p = 0$. (a) Cr atom fraction; (b) fluxes in the lattice reference frame; (c) relative deviation from equilibrium vacancy fraction.

unaffected by the value of k_m (Figure 4(a)).

Simulations done with varying k_m and k_p values show that flux profiles are mainly governed by k_m. Figure 5(a) shows pore fraction profiles obtained with varying k_p and a constant $k_m = 10$ s^{-1}. Porosity is predicted to develop close to the initial interface between the two alloys, on the Cr-rich side, at $z \cong$ 300-400 µm, where div J_{Va}^{lat} is maximum. The amplitude of the porosity peak increases with increasing k_p. Closer examination of pore fraction profiles shows that the amount of porosity depends on both k_p and k_m. Figure 5(b) shows the amplitude of the f_p peak as a function of both parameters. The porosity is seen to generally increase with increasing k_p; the effect of k_m is not monotonic, as a maximum in porosity is obtained for $k_m \cong 1\ s^{-1}$. This non-monotonicity results from two antagonistic effects: on the one hand, a larger k_m will consume more vacancies in regions of vacancy excess, and thereby reduce the supersaturation that would otherwise feed pore growth; this tends to oppose pore growth. On the other hand, a smaller k_m will hinder the generation of vacancies in undersaturated regions, which will increase the undersaturation, increase the μ_{Va} gradient and thereby lower the flux of vacancies towards supersaturated regions, in turn reducing the quantity of vacancies available for pore formation. The latter effect is demonstrated in Figure 5(c).

4.2 Binary system with strong Kirkendall effect: NiSi

Simulations in the NiSi system were conducted using thermodynamic and mobility data from Du and Schuster [57,58]. Figures 6 and 7 show the equilibrium vacancy fraction and the tracer and intrinsic diffusion coefficients of Si and Ni at 1200 °C. The value of $\overline{D}_{\mathrm{Ni}}$ varies by more than two orders of magnitude over the composition range of interest ($\max(\overline{D}_{\mathrm{Ni}})$ / $\min(\overline{D}_{\mathrm{Ni}}) \cong 285$), while $\overline{D}_{\mathrm{Si}}$ has a weaker composition dependence. Furthermore, $\overline{D}_{\mathrm{Si}}$ and $\overline{D}_{\mathrm{Ni}}$ vary with slopes of opposite signs: on the Ni-rich side, $\overline{D}_{\mathrm{Si}}$ is about 5 times larger than $\overline{D}_{\mathrm{Ni}}$, while on the Si-rich side, $\overline{D}_{\mathrm{Si}}$ is about 100 times smaller than $\overline{D}_{\mathrm{Ni}}$. These variations imply a strong and non-uniform Kirkendall effect in diffusion couples in the NiSi system, as illustrated below.

Simulations were done for a Ni/Ni-10Si (at. %) diffusion couple, 10 h at 1200 °C, with varying values of k_m and k_p. The results obtained with no porosity ($k_p = 0$) are presented first.

Figure 8 presents profiles of the Si atom fraction, fluxes and vacancy deviation from equilibrium obtained from the simulations with $k_p = 0$. With an ideal lattice ($k_m = +\infty$), the Si atom fraction profile is asymmetric (Figure 8(a)): diffusion is faster on the Si-rich side, because of the larger diffusivity of Ni on that side (see Figure 7). This is reflected in the fluxes (Figure 8(b)): J_{Ni}^{lat} is larger on the Si-rich side than it is on the Si-lean side. Furthermore, its amplitude is larger than that of J_{Si}^{lat} on the Si-rich side, while the reverse is true on the Si-lean side, again reflecting the diffusivity variations. As a result, J_{Va}^{lat} changes sign across the couple. The vacancy fraction is at equilibrium everywhere (Figure 8(c)), as expected.

Decreasing k_m has the same effect as that observed in the NiCr system: it produces vacancy supersaturation and undersaturation in regions of vacancy annihilation and generation, respectively. In Ni / Ni-10Si, div J_{Va}^{lat} changes sign more than once: this produces two regions of vacancy undersaturation around a central region of supersaturation, visible for $k_m = 1\ s^{-1}$ in Figure 8(c). Again, the y_{Va} profiles are sensitive to the size of the simulation box for lower k_m values. In partic-

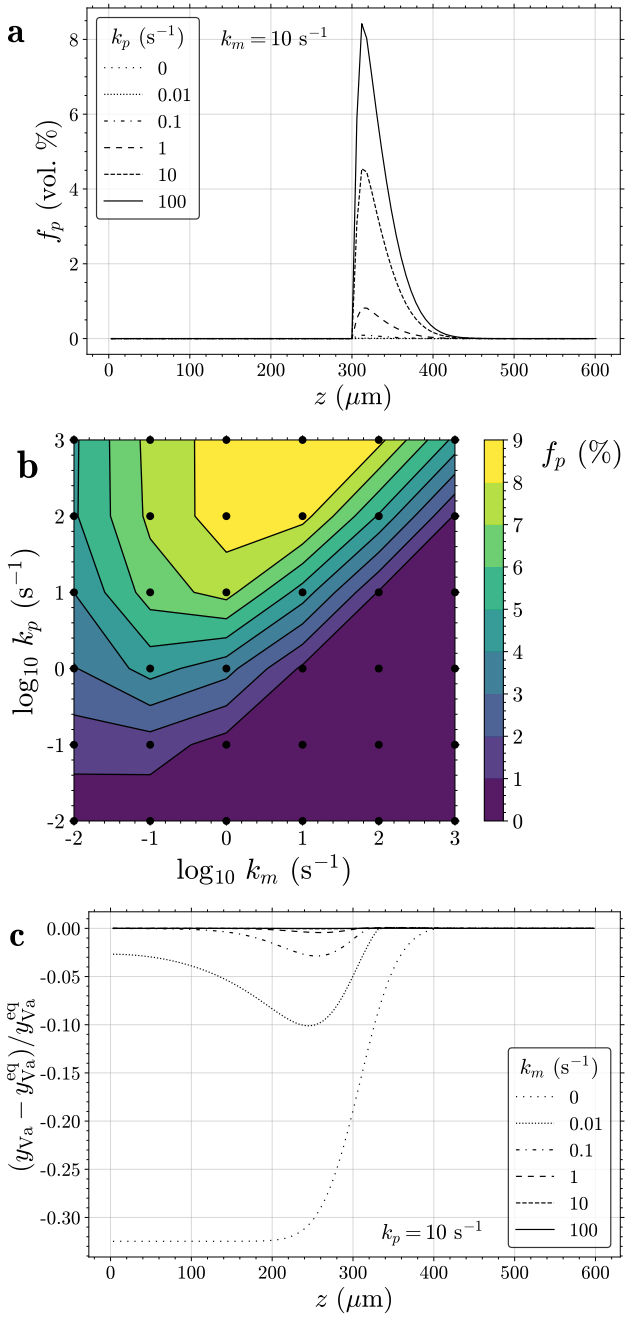

Figure 5: Simulation results for a Ni / Ni-30Cr (at. %) couple, after 10 h at 1200 °C. (a) Pore fraction profiles with $k_m = 10$ s^{-1}; (b) integral of the pore fraction profile as a function of k_m and k_p (each black circle represents a data point; the contours are obtained by interpolation); (c) relative deviation from equilibrium vacancy fraction with $k_p = 10$ s^{-1}.

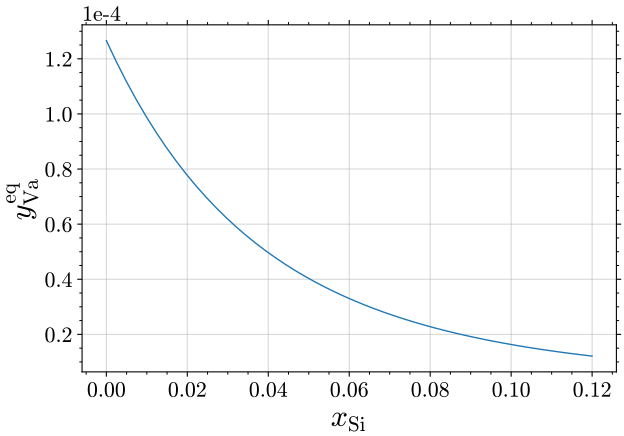

Figure 6: Equilibrium vacancy fraction in the Ni-Si system at 1200 °C, computed via Eqs. (21)–(22), using atom-vacancy interaction parameters from Shang et al [54] and Ni-Si data from Du and Schuster [57].

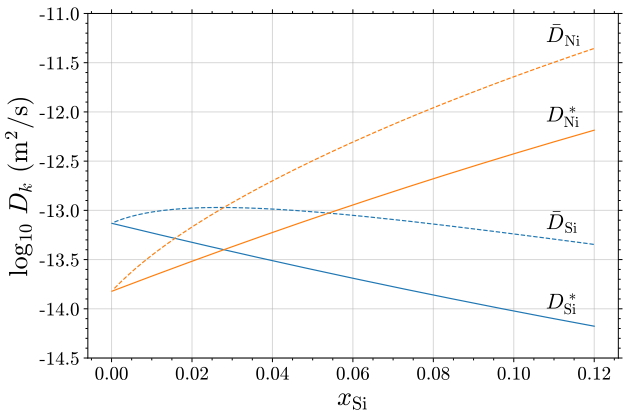

Figure 7: Tracer and intrinsic diffusion coefficients in the Ni-Si system at 1200 °C, computed using data from Du and Schuster [57,58].

ular, for $k_m = 0\ s^{-1}$, vacancy accumulation in the central region of the couple is so strong that the supersaturation reaches the left-hand side boundary, and in doing so, hides the effect of the vacancy depletion expected for $z < 200$ µm; the absence of undersaturation there is due to the limited size of the simulation box.

The μ_{Va} gradient generated by the vacancy supersaturation profile produces a driving force that opposes the Kirkendall effect, and the amplitude of J_{Va}^{lat} decreases until it reaches 0 for $k_m = 0$ (Figure 8 (b)). Since J_{Va}^{lat} changes sign across the couple, the effect of its decrease on J_{Si}^{lat} and J_{Ni}^{lat} is different on either side of the couple: J_{Ni}^{lat} decreases on the Si-rich side and slightly increases on the Si-lean side, while J_{Si}^{lat} follows opposite evolutions. The net result is that as k_m decreases, J_{Si}^{lat} and J_{Ni}^{lat} reach the same amplitude, and the amplitude of each of J_{Si}^{lat} and J_{Ni}^{lat} on the Si-rich side becomes comparable to those on the Si-lean side. In other words, the slowness of vacancy annihilation/generation inhibits the Kirkendall effect, and in doing so, cancels out the asymmetry in the fluxes that was due to the strong

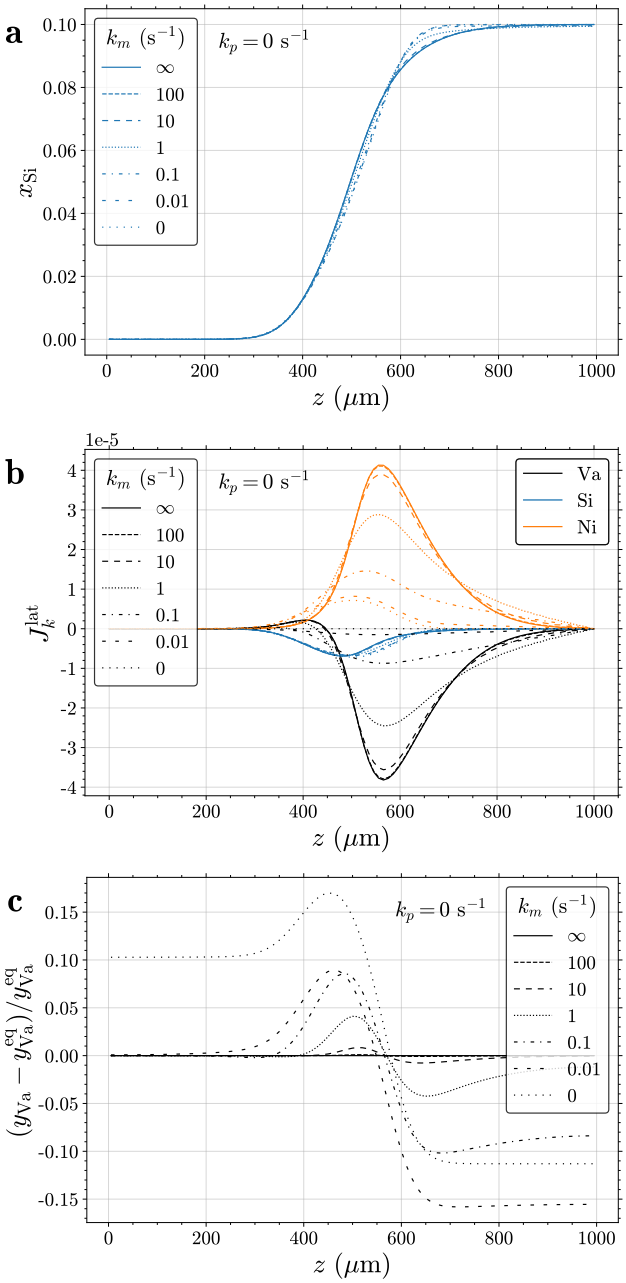

Figure 8: Simulation results for a Ni / Ni-10Si (at. %) couple, after 10 h at 1200 °C, with $k_p = 0$. (a) Si atom fraction; (b) fluxes in the lattice reference frame; (c) relative deviation from equilibrium vacancy fraction.

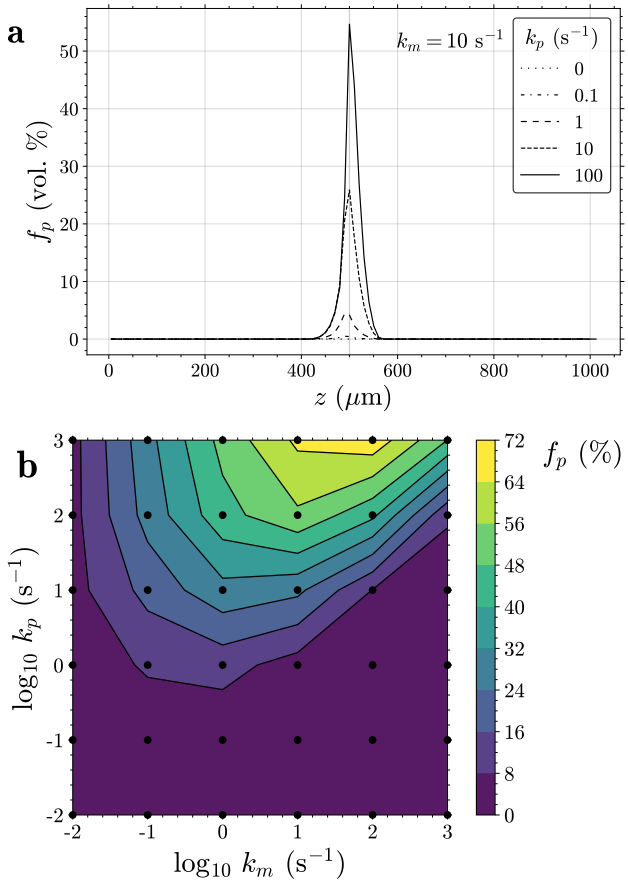

Figure 9: Simulation results for a Ni / Ni-10Si (at. %) couple, after 10 h at 1200 °C. (a) Pore fraction profiles with $k_m = 10$ s^{-1}; (b) maximum pore fraction as a function of k_m and k_p.

composition dependence of the intrinsic diffusivities. This side effect is also visible in the shape of the composition profiles: with values of k_m of 1 s^{-1} and below, the x_{Si} profile is nearly symmetric (Figure 8(a)).

Simulations done with varying k_m and k_p show the same effects observed with the Ni/Ni-30Cr couple. Figure 9(a) shows pore fraction profiles obtained with varying k_p and a constant $k_m = 10$ s^{-1}. Porosity is predicted to develop close to the initial interface between the two alloys, with a maximum amplitude slightly on the Si-lean side, where div J_{Va}^{lat} is maximum, and the vacancy supersaturation is the largest (Figure 8(c)). The pore fractions are about 10 times greater than those obtained with the Ni/Ni-30Cr couple. Figure 9(b) shows the amplitude of the f_p peak, where again the influence of the sink terms follows the trends observed with the NiCr couple.

5 Discussion

Qualitatively, the results reported here regarding the role of lattice sinks of arbitrary strength on substitutional diffusion are consistent with trends identified by previous

investigators (see e.g. Refs. [25,59,60] for lattice sinks with no pores, Refs. [32,34] for sinks associated with pores). The present work differs from these previous studies by evaluating the combined role of variable sink strengths in the lattice and at pore surfaces, and by demonstrating the interactions between the two types of sinks. The effect of including composition-dependent diffusivity data is also highlighted. Producing quantitative simulations requires realistic values of the sink strengths, k_m and k_p, that reflect the composition and microstructure of the alloys of interest. Accurate values are not readily available for the systems of interest but estimates are discussed now.

Fischer et al. [37] proposed a model of vacancy generation at dislocation jogs, which relates the sink strength to the jog density. With the present notations, their sink rate reads:

$$\alpha_m = -\frac{\mu_0 - \Omega_0 \sigma_H}{K \Omega_m} \ , \tag{56}$$

where σ_H is the hydrostatic stress, which is neglected here, and K is the bulk viscosity. If jogs are distributed evenly, the latter is given by [37]:

$$K = \frac{1}{2\pi a H A_0 \Omega_m^2} \ . \tag{57}$$

In Eq. (57), a is the lattice parameter, H is the number of jogs per unit volume, and A_0 is given by [37]:

$$A_0 = \frac{y_0}{y_0^{eq}} \frac{1}{RT f_0 \Omega_m} \sum_{k=1}^{n} y_k D_k^* \ , \tag{58}$$

where f_0 is the geometrical correlation factor ($f_0 = 0.7815$ for fcc crystals). The model used in the present work for transport coefficients, Eq. (30), amounts to making the approximation $f_0 \cong 1$; for consistency, this approximation is done here too. Let D_0^* be the tracer diffusion coefficient of vacancies, defined as:

$$D_0^* = \frac{1}{y_0} \sum_{k=1}^{n} y_k D_k^* \ . \tag{59}$$

(this definition differs from that used in Ref. [37]). The jog density is expressed as a function of the dislocation density ρ:

$$H = \frac{\rho}{n_p a} \ , \tag{60}$$

where n_p is the average jog spacing (number of sites between jogs) along a dislocation line. Using Eq. (23) for μ_0, the sink rate now reads:

$$\alpha_m = -\ln\left(\frac{y_0}{y_0^{eq}}\right) \frac{y_0}{y_0^{eq}} \frac{2\pi\rho}{n_p} y_0 D_0^* \ . \tag{61}$$

For $y_0 \cong y_0^{eq}$, if the logarithm is approximated by the first term of its Taylor series, this simplifies to:

$$\alpha_m = -\left(y_0 - y_0^{eq}\right) \frac{2\pi\rho}{n_p} D_0^* \ . \tag{62}$$

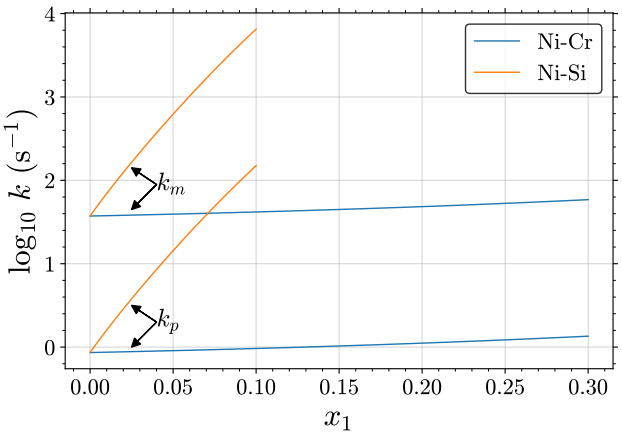

Figure 10: Sink strengths in the lattice, k_m, from Eq. (63) and at pore surfaces, k_p, from Eq. (71), evaluated for the Ni-Cr and Ni-Si systems at 1200 °C – see text for details. x_1 is the atom fraction of the alloying element, Cr or Si.

Equation (62) is analog to the linear form commonly used in the literature [10], $\alpha_m = -k_m\,(y_0 - y_0^{eq})$, with

$$k_m = \frac{2\pi\rho}{n_p} D_0^* \ . \tag{63}$$

In annealed fcc alloys, a typical dislocation density would be $\rho \cong 10^{12}$ m^{-2}. An order of magnitude estimate of the jog spacing in common metals is given in Ref. [61]: $n_p \cong 100$ at 1000 K, which, using their model, extrapolates to $n_p \cong 20$ at 1200 °C. As discussed in Ref. [37], different values of n_p can be arrived at depending on the method used to determine it. Given the use of approximate values for ρ and n_p, the results obtained here should be considered as order of magnitude estimates.

Values of the sink strengths calculated from Eq. (63) in the Ni-Cr and Ni-Si systems at 1200 °C are plotted in Figure 10. The composition dependence of k_m derives from that of D_0^*, and in turn from those of the tracer diffusion coefficients of the relevant species. Accordingly, k_m is nearly constant in the Ni-Cr system, while it has a strong composition dependence in the Ni-Si system. In both cases, the values obtained this way are large, relative to those used in the simulations shown in Section 4 – in other words, the values given by Eq. (63) correspond to conditions close to those of the ideal lattice, with relatively small deviations from equilibrium in terms of vacancy fractions.

An estimate for the sink strength at pore surfaces, k_p, is now obtained following the two-scale, quasi-steady-state approach of Gusak and Storozhuk [31]. Briefly, this approach relies on the distinction of a coarse-grained scale, where the diffusion problem is solved in the absence of pores, and a fine-grained scale, where pore growth is solved subject to boundary conditions imposed by the coarse-grained problem. Consider a uniform distribution of spherical pores with average pore spacing $2r_s$ and average pore radius r_p. The rate of vacancy annihilation at a pore surface is given by:

$$\dot{N}_p = J_0^{lat}\,(r_p)\,4\pi r_p^2. \tag{64}$$

The number of sites in the region of influence of a pore, defined as the sphere of

radius r_s centered on the pore center, is:

$$N = \frac{4}{3}\pi \left(r_s^3 - r_p^3\right) \frac{1}{\Omega_m}. \tag{65}$$

The sink rate is then:

$$\alpha_p = \frac{\dot{N}_p}{N} = \Omega_m J_0^{lat}\left(r_p\right) \frac{3r_p^2}{r_s^3 - r_p^3}. \tag{66}$$

The vacancy flux at the pore surface is then estimated by considering two boundary conditions. (1) At the pore surface, vacancies are at equilibrium. Taking into account the Gibbs-Thomson effect, this reads:

$$y_0\left(r_p\right) = y_0^{eq} \exp\left(\frac{2\gamma\Omega_m}{r_p RT}\right), \tag{67}$$

where γ is the surface energy. (2) Far away from the pore, the vacancy fraction is that of the coarse-grained diffusion problem, $y_0\left(z,\ t\right)$, simply noted y_0. With the present notations, the vacancy flux derived in Ref. [31] is:

$$J_0^{lat}\left(r_p\right) = \frac{D_0^*}{\Omega_m}\left(y_0\left(r_p\right) - y_0\right)\left(\frac{1}{L_0} + \frac{1}{r_p}\right), \tag{68}$$

where L_0 is the mean free path of vacancies in the presence of lattice sinks, given by:

$$L_0 = \sqrt{D_0^* \tau_m} = \sqrt{\frac{D_0^*}{k_m}}. \tag{69}$$

Using Eq. (63) for k_m yields $L_0 = \sqrt{\frac{n_p}{2\pi\rho}} \cong 1.8$ µm in the conditions of interest.

Using a typical surface tension of 1 J m^{-2}, the exponential in Eq. (67) decays rapidly and is close to one for r_p values above 10 nm. We are interested in the steady-state, where r_p is in the µm range. In these conditions, the Gibbs-Thomson effect is negligible and $y_0\left(r_p\right) \cong y_0^{eq}$. Introducing Eq. (68) in Eq. (66) then leads to:

$$\alpha_p = -D_0^*\left(y_0 - y_0^{eq}\right)\left(\frac{1}{L_0} + \frac{1}{r_p}\right)\frac{3r_p^2}{r_s^3 - r_p^3}\ . \tag{70}$$

Equation (70) takes the linear form $\alpha_p = -k_p\left(y_0 - y_0^{eq}\right)$, with

$$k_p = D_0^*\left(\frac{1}{L_0} + \frac{1}{r_p}\right)\frac{3r_p^2}{r_s^3 - r_p^3}\ . \tag{71}$$

Noting that the pore fraction is related to r_s and r_p via

$$f_p = \left(\frac{r_p}{r_s}\right)^3\ , \tag{72}$$

the pore sink strength can also be written:

$$k_p = D_0^*\left(\frac{1}{L_0} + \frac{1}{r_s f_p^{1/3}}\right)\frac{3}{r_s}\frac{f_p^{2/3}}{f_m}\ . \tag{73}$$

The evolution of k_p as pores develop follows from two opposite contributions visible in Eq. (73): as f_p increases, $J_0^{lat}(r_p)$ decreases, while the ratio of pore to metal volume increases. Overall, the latter contribution prevails, and k_p increases with increasing f_p.

Typical pore distributions in the conditions of interest can be described by $r_p = 5$ µm and $r_s = 20$ µm. These are then fed into Eq. (71) to evaluate k_p. Again, it is emphasized that the results obtained this way are order of magnitude estimates. In particular, Eq. (68) implies that pores be isolated, which requires $r_s \gg r_p$: this is obviously not respected in the conditions retained here. Values of k_p calculated from Eq. (71) in the Ni-Cr and Ni-Si systems at 1200 °C are plotted in Figure 10. Again the composition dependence is given by that of D_0^*. We note that the estimated k_p values are smaller than the k_m values by about 1.5 decades. Referring to Figures 5(b) and 9(b), this situation where $k_p < k_m$ is not favorable to the development of porosity. A quantitative evaluation of pore fractions expected with these sink strengths cannot be obtained by interpolation of the simulation results showed in Section 4 since the latter were obtained with constant sink strengths. At the composition mid-ranges (Ni-15Cr and Ni-5Si), one finds $k_m = 45\ s^{-1}$ and $k_p = 1\ s^{-1}$ in the NiCr couple, and $k_m = 620\ s^{-1}$ and $k_p = 14\ s^{-1}$ in the NiSi couple. Interpolation of the simulation results on this basis yields maximum pore fractions of 0.2 % and 3.8 % in the NiCr and NiSi couples, respectively.

Obtaining more accurate estimations of pore fractions will require using composition-dependent, time-dependent models of the sink strengths such as those outlined in this Section. Together with such simulations, dedicated experiments would be useful to assess the validity of the parameters entering these models (dislocation density, average jog and pore spacing), and discuss how these may vary from one alloy system to another. Such experiments are currently under way in our laboratory, and will be the object of a forthcoming publication.

6 Conclusions

The present work evaluates the development of non-equilibrium vacancy concentrations and of porosity associated with the Kirkendall effect, using critically assessed thermodynamic and mobility data. It shows how reducing the lattice sink strength slows down vacancy generation/annihilation, to a point where two elements of different intrinsic diffusivities diffuse at the same rate. The lattice sink strength plays two antagonistic roles with regards to pore formation. A higher sink strength leads to smaller vacancy supersaturation in regions of vacancy excess, which hinders pore growth: excess vacancies are consumed by lattice shift rather than by pore growth. A lower sink strength produces larger vacancy undersaturation in regions of vacancy deficit; the resulting vacancy potential gradient opposes vacancy diffusion toward the pore-forming region, which hinders pore growth as well. Our parametric study shows that a maximum pore growth is obtained with intermediate lattice sink strengths.

Our work highlights the influence of intrinsic diffusivities and their composition dependence on the Kirkendall effect. In the NiCr system, $\overline{D}_{\mathrm{Cr}}$ and $\overline{D}_{\mathrm{Ni}}$ are of similar amplitude, and each is weakly composition-dependent. Atom concentration profiles are nearly symmetric, and are not significantly affected by the vacancy excess and deficit that develop with finite sink strengths. On the other hand, in the

NiSi system, $\overline{D}_{\mathrm{Si}}$ and $\overline{D}_{\mathrm{Ni}}$ are strongly dissimilar, and each is strongly composition-dependent. This produces non-symmetric atom concentration profiles in ideal lattice conditions. Reducing the lattice sink strength significantly affects these profiles, as they become more symmetric.

In both systems, the maximum vacancy excess/deficit, obtained in the absence of vacancy sinks, is smaller than 30 %, relative to the local equilibrium concentration. This indicates that the effects associated with non-equilibrium vacancies should remain of limited amplitude. For instance, atom mobilities measured in a diffusion couple with finite sink strength are not expected to be significantly different from the mobilities measured in a tracer experiment.

Finally, this work provides a basis for the evaluation of the parameters involved in lattice sinks (dislocation density and jog spacing) from experimental data. In systems where intrinsic diffusivities bear a sufficiently strong composition dependence, the fact that atom concentration profiles are sensitive to excess/deficit vacancies may in principle be used to evaluate lattice sink strengths from diffusion couple experiments.

Acknowledgements

TG would like to thank A. Finel, Y. Le Bouar and A. Ruffini (ONERA/LEM) for stimulating discussions on the modeling of the Kirkendall effect. This work was funded in part by the Agence Nationale de la Recherche (France), grant number ANR-19-CE08–0004.

Appendix A: Equilibrium vacancy fraction

Let G_m be the Gibbs free energy per mole of metal,

$$G_m = \frac{G}{N - N_0} = \frac{G_M}{1 - y_0} \ . \tag{A.1}$$

The metal-pore equilibrium is achieved when [47–49]

$$\frac{\partial G_m}{\partial y_0} = 0. \tag{A.2}$$

After some manipulation, one can show that

$$\frac{\partial G_m}{\partial y_0} = \frac{\mu_0}{(1 - y_0)^2} \ . \tag{A.3}$$

We are interested in the metal phase, where the equilibrium vacancy fraction is orders of magnitude smaller than 1. We therefore make the approximation $y_0 \ll 1$ and the equilibrium condition, Eq. (19), simply becomes $\mu_0 = 0$.

Appendix B: Atom-vacancy interaction parameters

We follow the method by Abe et al. [48]. Consider the A-Va system, where A is an atom species and Va represents vacancies. The Gibbs energy per mole of lattice site is written:

$$G_M = y_A G_A + y_{Va} G_{Va} + RT \left(y_A \ln y_A + y_{Va} \ln y_{Va} \right) + y_A y_{Va} \Lambda_{AVa}, \tag{B.1}$$

where Λ_{AVa} represents non-ideal interactions between A and Va. We assume A–Va is a regular solution, i.e., Λ_{AVa} is composition-independent. Making the approximation $y_{Va} \ll 1$, the equilibrium condition, Eq. (19), is written

$$G_{Va} + RT \ln\left(y_{Va}^{eq}\right) + \Lambda_{AVa} = 0. \tag{B.2}$$

This yields

$$y_{Va}^{eq} = \exp\left(-\frac{G_{f,Va}^{A}}{RT}\right) \tag{B.3}$$

with $G_{f,Va}^{A} = G_{Va} + \Lambda_{AVa}$ the energy of formation of vacancies in A. If the latter is known, Λ_{AVa} can be evaluated. This is then repeated for all atom species of the multicomponent alloy considered.

Appendix C: Fluxes in the lattice reference frame

The derivation follows Van der Ven et al. [62]. We inject Eq. (25) into Eq. (26) to obtain

$$\sum_{i=0}^{n}\left(\text{grad}\ \mu_i \cdot \sum_{k=0}^{n} L_{ik}\right) = 0. \tag{C.1}$$

For Eq. (C.1) to be fulfilled for arbitrary chemical potentials, we must require [63]

$$\sum_{i=0}^{n} L_{ik} = 0 \qquad \forall k. \tag{C.2}$$

Equation (C.2) is then used to substitute all L_{k0} in Eq. (25), which yields the desired expression, Eq. (27).

Appendix D: Derivation of the continuity equations

Following Svoboda et al. [26,28], the mass balance is written

$$\begin{cases} \dot{N}_k = -W \cdot \text{div}\ J_k^{lat} & (k > 0) \\ \dot{N}_0 = -W \cdot \text{div}\ J_0^{lat} + \dot{N}. \end{cases} \tag{D.1}$$

Using Eq. (3), this is expressed in terms of site fractions:

$$\begin{cases} \dot{y}_k = -\Omega \cdot \text{div}\ J_k^{lat} - y_k \dfrac{\dot{N}}{N} & (k > 0) \\ \dot{y}_0 = -\Omega \cdot \text{div}\ J_0^{lat} - y_0 \dfrac{\dot{N}}{N} + \dfrac{\dot{N}}{N}. \end{cases} \tag{D.2}$$

With Eq. (13), we obtain

$$\begin{cases} \dot{c}_k = -\text{div}\ J_k^{lat} - c_k \dfrac{\dot{W}}{W} & (k > 0) \\ \dot{c}_0 = -\text{div}\ J_0^{lat} - c_0 \dfrac{\dot{W}}{W} + \dfrac{1}{\Omega}\dfrac{\dot{N}}{N}. \end{cases} \tag{D.3}$$

In deriving Eq. (D.3), we have also used the following relation,

$$\frac{\dot{W}}{W} = \frac{\dot{N}}{N} + \frac{\dot{\Omega}}{\Omega}, \tag{D.4}$$

which derives from Eq. (10) and reflects the fact that volume variations are due to variations in the number of lattice sites and in the molar volume. The term $\dot{\Omega}/\Omega$ in Eq. (D.4) cannot be directly evaluated. Instead, we note that combining Eqs. (1) and (9), the rate of volume variations can be decomposed into contributions from the metal and the pores, which are more easily accessed:

$$\frac{\dot{W}}{W} = f_m \left(\frac{\dot{N}}{N} + \frac{\dot{\Omega}_m}{\Omega_m} \right) + f_p \frac{\dot{W}_p}{W_p}. \tag{D.5}$$

The rate of volume variation can be expressed as the divergence of the lattice velocity:

$$\frac{\dot{W}}{W} = \text{div v}. \tag{D.6}$$

This yields

$$\begin{cases} \dot{c}_k = -\text{div}\, J_k^{lat} - c_k \,\text{div}\, v \qquad (k > 0) \\ \dot{c}_0 = -\text{div}\, J_0^{lat} - c_0 \,\text{div}\, v + \dfrac{1}{\Omega}\dfrac{\dot{N}}{N}. \end{cases} \tag{D.7}$$

The time derivatives in Eqs. (D.7) are material (or total) derivatives:

$$\dot{c}_k = \frac{Dc_k}{Dt} = \frac{\partial c_k}{\partial t} + v \cdot \text{grad}\ c_k. \tag{D.8}$$

Introducing Eq. (D.8) in Eqs. (D.7) yields the set of continuity equations used in Section 2.5, Eqs. (39).

Data availability

The raw/processed data required to reproduce these findings cannot be shared at this time due to time limitations. The source code used to produce all data will be distributed under an open license.

References

[1] J.-O. Andersson, T. Helander, L. Höglund, P. Shi, B. Sundman, Thermo-Calc & DICTRA, computational tools for materials science, Calphad. 26 (2002) 273–312. DOI: 10.1016/S0364–5916(02)00037–8
[2] M.S.A. Karunaratne, S.L. Ogden, S.D. Kenny, R.C. Thomson, A multicomponent diffusion model for prediction of microstructural evolution in coated Ni based

superalloy systems, Materials Science and Technology. 25 (2009) 287–299. DOI: 10.1179/174328408X355415
[3] M. Bensch, A. Sato, N. Warnken, E. Affeldt, R.C. Reed, U. Glatzel, Modelling of High Temperature Oxidation of Alumina-Forming Single-Crystal Nickel-Base Superalloys, Acta Materialia. 60 (2012) 5468–5480. DOI: 10.1016/j.actamat.2012.06.036
[4] J. Herrnring, B. Sundman, B. Klusemann, Diffusion-driven microstructure evolution in OpenCalphad, Computational Materials Science. 175 (2020) 109236. DOI: 10.1016/j.commatsci.2019.109236
[5] R. Pillai, A. Chyrkin, W.J. Quadakkers, Modeling in High Temperature Corrosion: A Review and Outlook, Oxid Met. 96 (2021) 385–436. DOI: 10.1007/s11085-021-10033-y
[6] T. Gheno, C. Rio, M. Ecochard, D. Texier, Alumina Failure and Post-failure Oxidation in the NiCoCrAlY Alloy System at High Temperature, Oxid Met. 96 (2021) 487–517. DOI: 10.1007/s11085–021–10060–9
[7] E.O. Kirkendall, Diffusion of Zinc in Alpha Brass, Trans. AIME. 147 (1942) 104–110.
[8] A.D. Smigelskas and E.O. Kirkendall, Zinc Diffusion in Alpha Brass, Trans. AIME. 171 (1947) 130–142.
[9] H. Nakajima, The discovery and acceptance of the Kirkendall Effect: The result of a short research career, JOM. 49 (1997) 15–19. DOI: 10.1007/BF02914706
[10] J. Philibert, Atom movements - Diffusion and mass transport in solids, Les Editions de Physique, Les Ulis, 1991
[11] F. Seitz, On the porosity observed in the Kirkendall effect, Acta Metallurgica. 1 (1953) 355–369. DOI: 10.1016/0001–6160(53)90112–6
[12] R.W. Balluffi, The supersaturation and precipitation of vacancies during diffusion, Acta Metallurgica. 2 (1954) 194–202. DOI: 10.1016/0001–6160(54)90159–5
[13] G.B. Stephenson, Deformation during interdiffusion, Acta Metallurgica. 36 (1988) 2663–2683. DOI: 10.1016/0001–6160(88)90114–9
[14] A. Gusak, B. Wierzba, M. Danielewski, Competition between Kirkendall shift and backstress in interdiffusion revisited – simple analytic model, Philosophical Magazine. 94 (2014) 1153–1165. DOI: 10.1080/14786435.2013.878053
[15] I. Daruka, I.A. Szabo, D.L. Beke, Cs. Cserhati, A. Kodentsov, F.J.J. van Loo, Diffusion-induced bending of thin sheet couples: Theory and experiments in Ti-Zr system, Acta Materialia. 44 (1996) 4981–4993. DOI: 10.1016/S1359–6454(96)00099–7
[16] J.A. Dantzig, W.J. Boettinger, J.A. Warren, G.B. McFadden, S.R. Coriell, R.F. Sekerka, Numerical modeling of diffusion-induced deformation, Metall and Mat Trans A. 37 (2006) 2701–2714. DOI: 10.1007/BF02586104
[17] L.S. Darken, Diffusion, Mobility and Their Interrelation through Free Energy in Binary Metallic Systems, Trans. AIME. 175 (1948) 184–194.
[18] J. Ågren, Diffusion in phases with several components and sublattices, Journal of Physics and Chemistry of Solids. 43 (1982) 421–430. DOI: 10.1016/0022-3697(82)90152-4
[19] J.-O. Andersson, J. Ågren, Models for numerical treatment of multicomponent diffusion in simple phases, Journal of Applied Physics. 72 (1992) 1350–1355. DOI: 10.1063/1.351745
[20] L. Höglund, J. Ågren, Analysis of the Kirkendall effect, marker migration

and pore formation, Acta Materialia. 49 (2001) 1311–1317. DOI: 10.1016/S1359-6454(01)00054-4
[21] R.A. Masumura, B.B. Rath, C.S. Pande, Analysis of Cu–Ni diffusion in a spherical geometry for excess vacancy production, Acta Materialia. 50 (2002) 4535–4544. DOI: 10.1016/S1359–6454(02)00273–2
[22] H. Strandlund, H. Larsson, Prediction of Kirkendall shift and porosity in binary and ternary diffusion couples, Acta Materialia. 52 (2004) 4695–4703. DOI: 10.1016/j.actamat.2004.06.039
[23] K. P. Gurov and A. M. Gusak, Description of the interdiffusion in alloys with an arbitrary power of vacancy sinks, Fiz. Met. Metalloved. 59, 1062–1066 (1985).
[24] D. Monceau, C. Petot, G. Petot-Ervas, Kinetic demixing profile calculation in oxide solid solutions under a chemical potential gradient, Solid State Ionics. 45 (1991) 231–237. DOI: 10.1016/0167–2738(91)90156–6
[25] G. Martin, C. Desgranges, Diffusion in crystals with nonconservative defects, Europhysics Letters 44 (1998) 150–155. DOI: 10.1209/epl/i1998–00449–1
[26] J. Svoboda, F.D. Fischer, P. Fratzl, A. Kroupa, Diffusion in multi-component systems with no or dense sources and sinks for vacancies, Acta Materialia. 50 (2002) 1369–1381. DOI: 10.1016/S1359–6454(01)00443–8
[27] I.V. Belova, G.E. Murch, Analysis of vacancies produced at non-equilibrium concentrations by interdiffusion, Philosophical Magazine. 85 (2005) 1191–1203. DOI: 10.1080/14786430412331331998
[28] J. Svoboda, F.D. Fischer, P. Fratzl, Diffusion and creep in multi-component alloys with non-ideal sources and sinks for vacancies, Acta Materialia. 54 (2006) 3043–3053. DOI: 10.1016/j.actamat.2006.02.041
[29] H.-C. Yu, D.-H. Yeon, A. Van der Ven, K. Thornton, Substitutional diffusion and Kirkendall effect in binary crystalline solids containing discrete vacancy sources and sinks, Acta Materialia. 55 (2007) 6690–6704. DOI: 10.1016/j.actamat.2007.08.031
[30] K.R. Elder, K. Thornton, J.J. Hoyt, The Kirkendall effect in the phase field crystal model, Philosophical Magazine. 91 (2011) 151–164. DOI: 10.1080/14786435.2010.506427
[31] A.M. Gusak, N.V. Storozhuk, Competition of K and F sinks during void formation, Phys. Metals Metallogr. 114 (2013) 197–206. DOI: 10.1134/S0031918X13030071
[32] C. Desgranges, F. Lequien, E. Aublant, M. Nastar, D. Monceau, Depletion and Voids Formation in the Substrate During High Temperature Oxidation of Ni–Cr Alloys, Oxid Met. 79 (2013) 93–105. DOI: 10.1007/s11085–012–9328–0
[33] B. Wierzba, Competition between Kirkendall and Frenkel effects during multicomponent interdiffusion process, Physica A. 403 (2014) 29–34. DOI: 10.1016/j.physa.2014.02.014
[34] P. Audigié, Modélisation de línterdiffusion et du comportement en oxydation cyclique de superalliages monocristallins à base de nickel revêtus dúne sous-couche γ-γ' riche en platine. Extension aux systèmes barrière thermique, PhD thesis, Institut National Polytechnique de Toulouse, 2015. https://www.theses.fr/2015INPT0054
[35] B. Wierzba, W. Skibiński, The interdiffusion in copper-nickel alloys, Journal of Alloys and Compounds. 687 (2016) 104–108. DOI: 10.1016/j.jallcom.2016.06.085
[36] C.-H. Xia, J. Kundin, I. Steinbach, S. Divinski, Model for non-equilibrium vacancy diffusion applied to study the Kirkendall effect in high-entropy alloys, Acta Materialia. 232 (2022) 117966. DOI: 10.1016/j.actamat.2022.117966
[37] F.D. Fischer, J. Svoboda, F. Appel, E. Kozeschnik, Modeling of excess vacancy annihilation at different types of sinks, Acta Materialia. 59 (2011) 3463–3472. DOI:

10.1016/j.actamat.2011.02.020
[38] H.-C. Yu, D.-H. Yeon, X. Li, K. Thornton, Continuum simulations of the formation of Kirkendall-effect-induced hollow cylinders in a binary substitutional alloy, Acta Materialia. 57 (2009) 5348–5360. DOI: 10.1016/j.actamat.2009.07.033
[39] H.-C. Yu, A.V. der Ven, K. Thornton, Simulations of the Kirkendall-Effect-Induced Deformation of Thermodynamically Ideal Binary Diffusion Couples with General Geometries, Metall and Mat Trans A. 43 (2012) 3481–3500. DOI: 10.1007/s11661–012–1299-x
[40] F.D. Fischer, J. Svoboda, Diffusion of elements and vacancies in multi-component systems, Progress in Materials Science. 60 (2014) 338–367. DOI: 10.1016/j.pmatsci.2013.09.001
[41] N. Saunders, A.P. Miodownik, CALPHAD (Calculation of Phase Diagrams): A Comprehensive Guide, Pergamon Press, 1998
[42] H. Lukas, S.G. Fries, B. Sundman, Computational Thermodynamics – The Calphad Method, Cambridge University Press, 2007
[43] W.A. Oates, S.-L. Chen, W. Cao, F. Zhang, Y.A. Chang, L. Bencze, E. Doernberg, R. Schmid-Fetzer, Vacancy thermodynamics for intermediate phases using the compound energy formalism, Acta Materialia. 56 (2008) 5255–5262. DOI: 10.1016/j.actamat.2008.07.002
[44] A.T. Dinsdale, A.V. Khvan, A. Watson, Critical Assessment 5: Thermodynamic data for vacancies, Materials Science and Technology. 30 (2014) 1715–1718. DOI: 10.1179/1743284714Y.0000000589
[45] P. Franke, Modeling of Thermal Vacancies in Metals within the Framework of the Compound Energy Formalism, J. Phase Equilib. Diffus. 35 (2014) 780–787. DOI: 10.1007/s11669-014-0348-0
[46] J. Rogal, S.V. Divinski, M.W. Finnis, A. Glensk, J. Neugebauer, J.H. Perepezko, S. Schuwalow, M.H.F. Sluiter, B. Sundman, Perspectives on point defect thermodynamics, Physica Status Solidi (b). 251 (2014) 97–129. DOI: 10.1002/pssb.201350155
[47] P.-W. Guan, Z.-K. Liu, A physical model of thermal vacancies within the CALPHAD approach, Scripta Materialia. 133 (2017) 5–8. DOI: 10.1016/j.scriptamat.2017.02.002
[48] T. Abe, K. Hashimoto, M. Shimono, Description of Thermal Vacancies in the CALPHAD Method, Materials Transactions. 59 (2018) 580–584. DOI: 10.2320/matertrans.M2017328
[49] J. Ågren, M. Hillert, Thermodynamic modelling of vacancies as a constituent, Calphad. 67 (2019) 101666. DOI: 10.1016/j.calphad.2019.101666
[50] J.R. Manning, Correlation factors for diffusion in nondilute alloys, Phys. Rev. B. 4 (1971) 1111–1121. DOI: 10.1103/PhysRevB.4.1111
[51] C.R. Harris et al., Array programming with NumPy, Nature. 585 (2020) 357–362. DOI: 10.1038/s41586–020–2649–2
[52] P. Virtanen et al., SciPy 1.0: fundamental algorithms for scientific computing in Python, Nat Methods. 17 (2020) 261–272. DOI: 10.1038/s41592–019–0686–2
[53] J.D. Hunter, Matplotlib: A 2D Graphics Environment, Computing in Science Engineering. 9 (2007) 90–95. DOI: 10.1109/MCSE.2007.55
[54] S.-L. Shang, B.-C. Zhou, W.Y. Wang, A.J. Ross, X.L. Liu, Y.-J. Hu, H.-Z. Fang, Y. Wang, Z.-K. Liu, A comprehensive first-principles study of pure elements: Vacancy formation and migration energies and self-diffusion coefficients, Acta Materialia. 109 (2016) 128–141. DOI: 10.1016/j.actamat.2016.02.031
[55] B.-J. Lee, On the stability of Cr carbides, Calphad. 16 (1992) 121–149. DOI:

10.1016/0364–5916(92)90002-F
[56] B. Jönsson, Assessment of the mobilities of Cr, Fe and Ni in binary fcc Cr-Fe and Cr-Ni alloys, Scandinavian Journal of Metallurgy. 24 (1995) 21–27.
[57] Y. Du, J.C. Schuster, Experimental investigations and thermodynamic descriptions of the Ni-Si and C-Ni-Si systems, Metall Mater Trans A. 30 (1999) 2409–2418. DOI: 10.1007/s11661–999–0249–8
[58] Y. Du, J.C. Schuster, Assessment of Diffusional Mobilities of Cr, Ni, and Si in fcc Cr-Ni-Si Alloys, Zeitschrift Für Metallkunde. 92 (2001) 28–31.
[59] F.D. Fischer, J. Svoboda, Substitutional diffusion in multicomponent solids with non-ideal sources and sinks for vacancies, Acta Materialia. 58 (2010) 2698–2707. DOI: 10.1016/j.actamat.2010.01.003
[60] J. Svoboda, F.D. Fischer, Modelling of the influence of the vacancy source and sink activity and the stress state on diffusion in crystalline solids, Acta Materialia. 59 (2011) 1212–1219. DOI: 10.1016/j.actamat.2010.10.054
[61] A.J. Ardell, H. Reiss, W.D. Nix, Statistics of Jogs on Dislocations at Equilibrium, Journal of Applied Physics 36 (1965) 1727–1732. DOI: 10.1063/1.1703117
[62] A. Van der Ven, H.-C. Yu, G. Ceder, K. Thornton, Vacancy mediated substitutional diffusion in binary crystalline solids, Progress in Materials Science. 55 (2010) 61–105. DOI: 10.1016/j.pmatsci.2009.08.001
[63] K.W. Kehr, K. Binder, S.M. Reulein, Mobility, interdiffusion, and tracer diffusion in lattice-gas models of two-component alloys, Phys. Rev. B. 39 (1989) 4891–4910. DOI: 10.1103/PhysRevB.39.4891